# Multifunctional Origami Patch for Minimally Invasive Tissue Sealing

**Sarah J. Wu**[#],
Department of Mechanical Engineering, Massachusetts Institute of Technology, Cambridge, MA 02139, USA

**Hyunwoo Yuk**[#],
Department of Mechanical Engineering, Massachusetts Institute of Technology, Cambridge, MA 02139, USA

**Jingjing Wu**,
Department of Mechanical Engineering, Massachusetts Institute of Technology, Cambridge, MA 02139, USA

**Christoph S. Nabzdyk**,
Department of Anesthesiology and Perioperative Medicine, Mayo Clinic, Rochester, MN 55905, USA

**Xuanhe Zhao**[*]
Department of Mechanical Engineering, Massachusetts Institute of Technology, Cambridge, MA 02139, USA; Department of Civil and Environmental Engineering, Massachusetts Institute of Technology, Cambridge, MA 02139, USA

## Abstract

For decades, bioadhesive materials have garnered great attention due to their potential to replace sutures and staples for sealing tissues during minimally invasive surgical procedures. However, the complexities of delivering bioadhesives through narrow spaces and achieving strong adhesion in fluid-rich physiological environments continue to present substantial limitations to the surgical translation of existing sealants. In this work, we introduce a new strategy for minimally invasive tissue sealing based on a multilayer bioadhesive patch, which is designed to repel body fluids, form fast, pressure-triggered adhesion with wet tissues, and resist biofouling and inflammation. The multifunctional patch is realized by a synergistic combination of three distinct functional

[*] zhaox@mit.edu.

Supporting Information
Supporting Information is available from the Wiley Online Library or from the author.

layers: (i) a micro-textured bioadhesive layer, (ii) a dynamic, blood-repellent hydrophobic fluid layer, and (iii) an antifouling zwitterionic non-adhesive layer. The patch is capable of forming robust adhesion to tissue surfaces in the presence of blood, and exhibits superior resistance to bacterial adhesion, fibrinogen adsorption, and in vivo fibrous capsule formation. By adopting origami-based fabrication strategies, we demonstrate that the patch can be readily integrated with a variety of minimally invasive end effectors to provide facile tissue sealing in ex vivo porcine models, offering new opportunities for minimally invasive tissue sealing in diverse clinical scenarios.

## Table of Contents

A multifunctional patch presents new opportunities for sealing tissues in minimally invasive surgeries. Integration of a dynamic hydrophobic fluid layer, a micro-textured bioadhesive layer, and a zwitterionic-interpenetrated elastomer layer enables the patch to be applied in fluid-rich environments, maintain a robust seal, and minimize biofouling and inflammation. The patch can be adapted to suit a range of clinical applications by employing origami-based design strategies for various surgical end effectors.
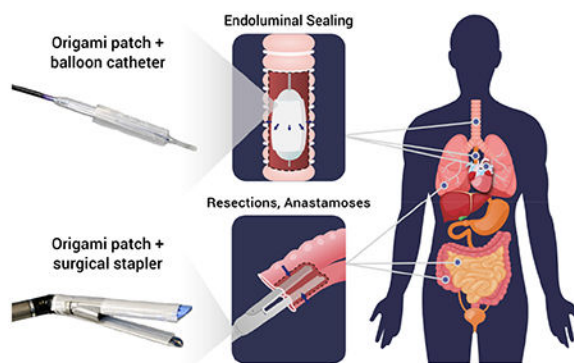


### Keywords

Bioadhesive; antifouling; origami; minimally invasive surgery; wound sealing

The ability to connect tissues is one of the cornerstones of general surgery. To this end, the traditional strategies of applying mechanical fasteners (i.e., sutures and staples) remain the current standards for sealing and repairing tissues in both open and minimally invasive surgery. However, these modalities have inherent drawbacks. Suturing entails complex manipulations which are timeconsuming and require a high level of surgical skill, making it disadvantageous during emergency scenarios. Meanwhile, surgical staplers are associated with an increasing number of adverse events caused by complications such as staple malformations and stapler misfirings.[1] Moreover, both sutures and staples can be mechanically damaging to tissues and are prone to dehiscence, leakage, and inflammation. [2,3] Associated postoperative complications, such as anastomotic leaks and fibrous adhesion formation with surrounding organs, can result in devastating clinical consequences for patients and often require subsequent readmission surgeries to achieve definitive surgical repair.[4,5] The challenges associated with sutures and staples are further amplified in

minimally invasive settings, during which the use of endoscopic equipment typically limits visualization, depth perception, range of motion, and haptic feedback.[6] Thus, although recent advances in surgical equipment have focused on evolving surgery toward less invasive techniques, tissue sealing remains a prevailing challenge.

In light of these shortcomings, bioadhesive materials have gained great attention as promising alternatives or adjuncts to sutures and staples for closing defects and attaching devices to organs.[2,3,7–14] However, most existing bioadhesives struggle to meet the functional requirements needed for practical use in minimally invasive surgery (Figure S1 and Supplementary Table 1). Most bioadhesives are available in the forms of liquids and glues, which can be easily displaced or diluted in dynamic and wet physiological environments.[3] Additionally, many bioadhesives suffer from contamination in the presence of body fluids such as blood and mucus, which render them ineffective before they can be maneuvered to the target tissues.[15] Several bioadhesives incorporate external-stimuli-based adhesion activation such as ultraviolet (UV) light crosslinking to offer improved controllability.[16,17] However, the requirement of external activation sources can hinder their usability by introducing additional complex and timeconsuming procedures. Furthermore, many bioadhesive precursors solidify into rigid polymers that are less stretchable and much stiffer than the adhered soft tissues, resulting in an adhesive-to-host compliance mismatch.[18] These limitations are often associated with relatively low adhesion strength and slow adhesion formation.[13,19] Additional clinical concerns include inflammatory responses, such as postoperative adhesion formation, and perioperative infectious complications.[3]

Here, we introduce a new strategy for tissue sealing and repair based on a multilayer tissue sealing patch, which synergistically combines three core functionalities to address the above-mentioned limitations (Figure 1): body fluid resistance, strong on-demand adhesion to wet tissues, and antifouling behavior. To achieve these properties, the patch integrates three distinct functional layers: (i) a micro-textured bioadhesive layer, (ii) a dynamic, blood-repellent hydrophobic fluid layer, and (iii) an antifouling zwitterionic non-adhesive layer. Notably, the material properties of the multilayer patch make it amenable to origami-inspired fabrication methods which endow it with a high degree of customizability. This ability to adopt customized form factors enables surgical application through a variety of deployment mechanisms driven by different surgical end effectors, offering a promising solution to a wide range of clinical indications (Figure 1b).

The multilayer composition of the tissue sealing patch is illustrated in Figure 1a. The patch comprises a bioadhesive layer sandwiched between an infused hydrophobic fluid layer and an antifouling non-adhesive layer. The hydrophobic fluid layer serves as a protective barrier which prevents the adhesive layer from becoming contaminated in the presence of body fluids by repelling blood and other immiscible contaminants. Micro-texturing of the bioadhesive interface promotes the infiltration of the fluid layer through stabilizing capillary forces.[20,21] Here, silicone oil has been employed as the hydrophobic fluid agent due to its chemical stability, established internal use as a lubricant for medical devices, and favorable wettability to the bioadhesive material.[22] Due to the contributing effect of substrate micro-structures, the hydrophobic fluid layer can be stably maintained during navigation through

fluid-rich environments, preserving the adhesive capacity of the underlying bioadhesive layer. Only under sufficient pressure does the textured bioadhesive surface undergo shear-driven dewetting, allowing for triggered de-protection of the bioadhesive layer. The pressure threshold for dewetting can be actively applied by pressing against tissue surfaces in order to (1) expel the oil and (2) allow the then-exposed bioadhesive material to adhere to the tissue (Figure 1c).

For the bioadhesive layer, we employ a double network material comprised of poly(acrylic acid) grafted with *N*-hydroxysuccinimide ester (PAA-NHS ester) and chitosan (Figure 1a). [13] This bioadhesive material forms fast and strong adhesion to wet tissues by adopting a dry-crosslinking mechanism. When the dry bioadhesive layer comes into contact with a wet tissue surface, it quickly absorbs the interfacial water and forms physical bonds (e.g., hydrogen bonds) within seconds (Figure 1c).[13,23] Subsequent formation of covalent bonds between the NHS ester groups and primary amine groups on the tissue surface further improves the adhesion strength and stability of the bioadhesive. Upon hydration and adhesion on wet tissues, the bioadhesive layer becomes a hydrogel with mechanical compliance and stretchability comparable to those of soft tissues.[13,24] To introduce micro-texture into the adhesive surface of the bioadhesive layer, microparticles of the bioadhesive material were produced by cryogenic grinding and embedded into the flat surface of a bioadhesive substrate. A three-dimensional (3D) reconstruction of confocal micrographs taken at the interface of the micro-textured bioadhesive (prepared using green fluorescent fluorescein-labeled chitosan) adhered to a gelatin hydrogel tissue phantom (prepared using red fluorescent Rhodamine Red™-labelled microbeads) shows the conformal adhesion interface between the micro-textured bioadhesive and the gelatin hydrogel (Figure S2b).

To mitigate biofoulings and postoperative inflammation, we integrate a zwitterionic-interpenetrated elastomer layer on the non-adhesive face of the patch (Figure 1a). Zwitterionic polymers have been found to have excellent antifouling properties.[25–29] Their unique ability to resist foulant adsorption is attributed to the presence of cationic and anionic groups in net neutral polymer chains, which promote the formation of a tight hydration shell while minimally disrupting the hydrogen-bonding structure of free water molecules (Figure 3a).[25,28] Disturbance of this hydration shell carries a high energy cost which precludes the surface adsorption of bacteria and biomolecules associated with inflammatory responses such as infection, blood coagulation, and postoperative adhesion formation. However, zwitterionic hydrogels typically suffer from poor mechanical properties such as low toughness and stretchability, which can be detrimental for their long-term robustness and stability in dynamic physiological environments.[30] To achieve a tough and stretchable antifouling layer for the patch, we interpenetrate zwitterionic polymers (i.e., poly(sulfobetaine methacrylate) (PSBMA)) into the surface of a thin film of hydrophilic polyurethane (PU) to synergistically combine the antifouling capacity of the zwitterionic moieties and the mechanical robustness of PU (Figure S3).[31] The resultant zwitterionic-interpenetrated PU layer exhibits superior mechanical properties (fracture toughness around 420 J m$^{-2}$ and stretchability over 3.5 times of the original length) compared to pure zwitterionic PSBMA hydrogels (fracture toughness around 0.35 J m$^{-2}$ and stretchability less than 1.5 times of the original length) (Figure 3c and Figure S4). To verify the presence of polysulfobetaines in the treated PU film, the surface was characterized by Fourier transform

infrared (FTIR) spectroscopy (Figure 3b). Compared to pristine PU, the FTIR spectrum for the zwitterionic-interpenetrated PU shows strong absorbance peaks at 1020 $cm^{-1}$ and 1180 $cm^{-1}$, which correspond to vibrations of the sulfonate group ($-SO_3$) present in the sulfobetaine moiety (Figure 3b).[30,31] The zwitterionic layer is integrated with the bioadhesive layer by using a thin coat of hydrophilic polyurethane solution to bond the two layers at the interface. The fully integrated multilayer patch takes the form of a thin and flexible polymer film in the dry state (Figure 1e), while it becomes a highly stretchable (stretchability over 5.5 times of the original length), soft (shear modulus around 70 kPa), and tough (fracture toughness around 2,100 J $m^{-2}$) hydrogel in the swollen state after forming adhesion on wet tissues (Figure S5).

To evaluate the protective capacity of the hydrophobic fluid layer, we exposed samples of the patch with and without silicone oil to blood and compared their fouling behaviors (Figure 2a). When submerged in a porcine blood bath, the patch without the silicone oil layer is immediately wetted by the blood and loses its adhesive capability, whereas the patch with the protective silicone oil layer resists blood contamination and remains intact (Figure 2a and Figure S6). To further investigate the effect of surface micro-texture on the stability of the fluid layer, we vigorously shook multilayer patches with flat and micro-textured bioadhesive surfaces in a porcine blood bath. While the multilayer patch with a flat bioadhesive surface shows substantial blood contamination after shaking, the patch comprising a micro-textured surface exhibits robust protection of the bioadhesive layer against vigorous blood flow (Figure 2b and Movie S1), supporting the significance of the micro-textured design of the bioadhesive layer in order to achieve stable contaminant-repellent properties.[20]

As the patch is brought in contact with a tissue substrate, applying pressure drives expulsion of the hydrophobic fluid layer from between the two solid surfaces. The exposed bioadhesive layer is then able to adhere to the tissue surface via the dry-crosslinking mechanism described above (Figure 1c). However, during this pressure-driven dewetting of the bioadhesive layer, it is possible for residual interfacial blood and oil to coalesce and remain entrapped at the interface, forming small non-adhered regions (Figures S8–S10). If substantial pockets of blood or oil become entrapped at the interface, the strength of the adhesive bond between the patch and the tissue can deteriorate. The amount of entrapped fluid is contingent on the pressure applied during compression of the multilayer patch against the tissue surface. To determine the optimal pressure conditions for removing interfacial blood and maximizing the area of adhesion, we quantified the amount of residual blood entrapped between patches and gelatin hydrogel tissue phantoms which were adhered under varying applied pressures while covered with porcine blood (Figures S7a–b and S8). We also measured the adhesive shear strength of patches adhered to blood-covered porcine skin tissues which were adhered under the same varying pressures (Figure S7c and S10). As the applied pressure increases, the area of entrapped blood decreases while the adhesive shear strength increases (Figure S7). When the applied pressure exceeds 77.5 kPa, the amount of entrapped blood and the adhesive shear strength both reach plateau values, indicating that a threshold pressure of 77.5 kPa can effectively repel most of the interfacial blood and activate optimal adhesion of the multilayer patch. Notably, this level of pressure

(i.e., around 100 kPa) can be readily applied by surgical end effectors such as staplers and balloons.[33–35]

To quantitatively evaluate the ability of the multilayer patch to form adhesion in blood, we adhered samples of the patch with porcine skin tissues submerged in a blood bath using an applied pressure of 77.5 kPa, and then performed 180-degree peel tests (ASTM F2256), lap-shear tests (ASTM F2255), and tensile tests (ASTM F2258) to measure the interfacial toughness, shear strength, and tensile strength of the adhered samples, respectively (Figures S11 and S12). We also measured the interfacial toughness, shear strength, and tensile strength of porcine skin tissues adhered using various commercially-available tissue adhesives including fibrin-based Tisseel, albumin-based Bioglue, polyethylene glycol (PEG)-based Coseal, and cyanoacrylate-based Histoacryl (Figure 2c). Compared to these commercially-available tissue adhesives, the multilayer patch resists blood contamination and achieves significantly higher interfacial toughness ($536.7 \pm 93.4$ J m$^{-2}$), shear strength ($56.1 \pm 4.7$ kPa), and tensile strength ($65.0 \pm 8.0$ kPa) (Figure 2c).

To characterize the antifouling performance of the zwitterionic layer, we investigated the patch's capability to mitigate *in vitro* bacterial adhesion, *in vitro* fibrinogen adsorption, and *in vivo* fibrous capsule formation (Figure 3d–j). Bacterial attachment to implanted materials can lead to biofilm formation and surgical site infection, which cause significant patient morbidity and substantial healthcare costs due to the need for additional procedures and antimicrobial therapies. To evaluate the antimicrobial performance of the zwitterionic layer, various patches with non-adhesive faces comprised of a hydrophobic polymer (polydimethylsiloxane, PDMS), a hydrophilic polymer (pristine hydrophilic PU), and the zwitterionic-interpenetrated elastomer were incubated with a green-fluorescent protein (GFP)-expressing *Escherichia coli* (*E. coli*). After 24 hours of incubation, the density of adhered *E. coli* on each surface was examined using fluorescent microscopy and measured in ImageJ (Figure 3d). In contrast to the patches featuring hydrophobic (~ 1,370 counts mm$^{-2}$) and hydrophilic non-adhesive layers (~ 1,360 counts mm$^{-2}$), the patch with the zwitterionic layer exhibits a significantly lower level of *E. coli* adhesion (~ 0.9 counts mm$^{-2}$) (Figure 3e).

We further evaluated the antifouling performance of the zwitterionic layer in blood by evaluating its capacity to resist the adsorption of fibrinogen in porcine whole blood. Surface attachment of fibrinogen leads to the formation of a fibrin meshwork, which serves as the basis of a blood clot. Thus, the surface coverage of fibrin can indicate the potential for a biomaterial to induce platelet accumulation, activation, and thrombus formation, which are undesirable for applications in which the bioadhesive interfaces with a bloodstream. Samples with non-adhesive layers comprised of a hydrophobic polymer (PDMS), a hydrophilic polymer (pristine hydrophilic PU), and the zwitterionic-interpenetrated elastomer were submerged in a blood bath containing heparinized porcine whole blood spiked with Alexa Fluor 488-tagged fibrinogen following a previously reported protocol. [22,36] After 60 min of incubation, the samples were fixed and the areal coverage of fibrin was compared among the different samples. Similar to the results for bacterial adhesion, the patch with the zwitterionic layer shows significantly lower levels of fibrin deposition (~0.1% areal coverage) compared to the patches with hydrophobic (~3.09% areal coverage) and

hydrophilic faces (~2.16% areal coverage) (Figure 3f–g). These results reflect a lower thrombogenic risk associated with the zwitterionic material in contact with whole blood.

To evaluate the biocompatibility and *in vivo* antifouling performance of the multilayer patch, we compared *in vivo* inflammation in rats in response to implanted patches with non-adhesive layers comprised of a hydrophobic polymer (PDMS), a hydrophilic polymer (pristine hydrophilic PU), and the zwitterionic-interpenetrated elastomer. Samples were implanted in the dorsal subcutaneous pockets of rats. At time points of 2 and 4 weeks following implantation, the tissues were collected and fixed for histological analysis and the thickness of the fibrous capsule around each implant was measured (Figure 3h–j). The formation of a thick fibrotic encapsulation around the surgical site is highly undesirable and can result in complications such as organ stricture and postoperative adhesions.[37,38] After 2 weeks of implantation, histological analysis shows that the patch with the zwitterionic layer exhibits a significantly thinner fibrous capsule around the patch (145 ±29 μm) compared to the patches with hydrophobic (574 ±125 μm) and hydrophilic polymer layers (185 ±16 μm) (Figure 3h–j). After 4 weeks of implantation, the patch with the zwitterionic layer maintains a similar thickness of fibrous capsule around the patch (135 ± 7 μm) to the 2-week results, whereas the patches with hydrophobic (1163 ± 138 μm) and hydrophilic (307 ± 73 μm) polymer layers exhibit significantly thicker fibrous capsules than their respective 2-week results (Figure 3i–j). In summary, these results suggest that the zwitterionic layer of the multilayer patch possesses favorable capacities to resist a range of perioperative and postoperative complications including bacterial adhesion, thrombus formation, and fibrotic encapsulations.

To further confirm the *in vivo* biocompatibility of the multilayer patch, histological images of the implanted samples were submitted for histological analysis and evaluated by a blinded pathologist (Figure S13). The degree of inflammation at the implantation site for the zwitterionic layer-containing patch received average scores of 1.33 and 1.67 after 2 and 4 weeks, respectively, which fall within the "very mild" to "mild" inflammation range. These results indicate that the multilayer patch elicits low levels of acute and chronic inflammation. Because the bioadhesive layer is comprised of PAA-NHS ester crosslinked with biodegradable linkages and the biopolymer chitosan, it can be left to undergo enzymatic biodegradation within the body if it is intended to be implanted without recurrent surgery (Figure S14).[13] The degradation rate can be tuned by changing the type of biopolymer used in the bioadhesive material (e.g., gelatin or alginate instead of chitosan) or the ratio of crosslinking agent used.

To explore the translational potential of the multilayer patch in minimally invasive surgery, we demonstrate two different deployment strategies (balloon catheter and surgical stapler) for applying the patch using existing minimally invasive surgical instruments (Figure 4). The multilayer patch can be customized to adopt diverse form factors owing to its thin, paper-like form and the material properties of its constituents. At room temperature, the dry bioadhesive layer of the patch is in the glassy state. As a result, a folded patch can maintain the folded hinges due to plastic deformation, making the patch amenable to origami-based designs (Figure 4a).[39–41] Hydration of the bioadhesive material, which occurs upon contact with wet tissues, lowers the glass transition temperature and causes the material to transit

into the rubbery state. This transition releases the plastic deformation at the folded hinges, and allows the patch conform to the tissue substrate. These properties enable the patch to undertake versatile geometries to suit various end effectors, such as balloon catheters and endoscopic staplers, and to form fluid-tight seals with curved and irregular tissue surfaces.

One such minimally invasive application enabled by the multilayer patch is the endoluminal sealing of tube-shaped organs and structures (e.g., trachea, esophagus, and vessels) via balloon catheters. For balloon catheter-based delivery and application, the patch is folded into a sleeve circumscribing the uninflated balloon, with the hydrophobic fluid layer oriented outward (Figure 4b). The sleeve unfurls upon inflation of the balloon, expanding to meet the walls of the hollow organ or vessel (Figure 4c). As the inflation pressure of the balloon increases, the radial pressure exerted by the balloon compresses the patch against the tissue wall, triggering the de-protection and adhesion of the bioadhesive layer (Figure 5a). We demonstrate that the proposed concept is readily applicable to a variety of surgical sites, exemplified in *ex vivo* experiments in which different sizes of balloon catheters were utilized to seal defects in a porcine trachea, esophagus, and aorta. Insertion and expansion of a Foley catheter (ReliaMed) outfitted with an origami patch sleeve resulted in the airtight sealing of a porcine trachea with a 5-mm circular transmural defect, immediately restoring the inflation capability of the lungs (Figure 5b and Movie S2). Similarly, adapting the dimensions of the origami sleeve to fit an esophageal balloon catheter (Boston Scientific) enabled rapid and fluid-tight sealing of a 5-mm circular transmural defect in a porcine esophagus (Figure 5c and Movie S3).The Foley catheter-based application method was further used to achieve hemostatic sealing of a 5-mm circular defect in an aorta (Figure 5d and Movie S4). The esophageal and aortic seals achieved using this strategy withstood the pumping of water and blood, respectively, at supraphysiological pressures over 300 mm Hg.

In addition to endoluminal sealing method using balloon catheters, we demonstrate that the multilayer patch can be integrated with an articulating endoscopic stapler (Ethicon) to provide a linear seal (Figure 6). This strategy of tissue repair could be useful for broader surgical applications such as anastomoses and resections. To enable stapler-based minimally invasive delivery, the multilayer patch is cut into various-sized strips and loaded in a folded origami sleeve designed to wrap around the anvil and cartridge units of the stapler (Figure 6a). Once the stapler jaws are positioned around the site of the tissue injury, actuation of the stapler compresses the multilayer patches against the tissue surface, triggering adhesion and sealing of the defect (Figure 6a). Using this method, the multilayer patch achieved rapid, fluid-tight sealing of a 5-mm circular transmural defect in a segment of an *ex vivo* porcine intestine (Figure 6a–b and Movie S5). To further simulate the stapler-based application in a minimally invasive surgical setting, sealing of an injured porcine intestine was repeated inside a dark chamber using a patch-loaded stapler inserted through ports and endoscopic camera footage to guide the process. (Figure 6c and Movie S5). As represented by these *ex vivo* demonstrations, the multilayer patch can potentially serve as a primary sealing and repair modality for various organ defects. Alternatively, it can act as an adjunct on top of a suture or staple line to support an anastomosis, especially in patients at high risk of anastomotic failure.

In this work, we have introduced a versatile tissue sealing patch which is capable of achieving rapid and robust tissue adhesion in body fluid-rich environments and mitigating a range of perioperative and postoperative complications such as infection, thrombus formation, and fibrotic encapsulations. While the full set of functionalities achieved by the multilayer patch make it an advantageous tissue sealant for surgery in general, its properties are particularly significant for use in minimally invasive surgery. Taking advantage of the material properties and paper-like form factor of the patch, we demonstrate that origami-based manufacturing techniques can be adopted to integrate the patch with various surgical end effectors for deployment in diverse minimally invasive procedures. Given the versatility and unique bioadhesive capability of the multilayer patch, it holds the potential to overcome current translational barriers in surgery and facilitate the broader adoption of less damaging and less invasive surgical techniques.

## Experimental Section

### Preparation of the bioadhesive layer:

30 w/w % acrylic acid, 2 w/w % chitosan (HMC+ Chitoscience Chitosan 95/500, 95 % deacetylation), 1 w/w % acrylic acid N-hydroxysuccinimide ester, 0.2 w/w % α-ketoglutaric acid, and 0.05 w/w % Poly(ethylene glycol) dimethacrylate) (PEGDMA; Mn = 550) were dissolved in deionized water. For fluorescent microscopic visualization of the bioadhesive layer, fluorescein-labeled chitosan was used. The precursor solution was poured on a glass mold with spacers (the thickness is 210 μm unless otherwise mentioned) and cured in a UV chamber (284 nm, 10 W power) for 30 min. Right after curing, dry bioadhesive microparticles were sifted through a 100 μm sieve over the surface of the bioadhesive hydrogel. The resulting bioadhesive hydrogel with surface-embedded microparticles was then thoroughly dried and sealed in plastic bags with desiccant (silica gel packets) and stored at −20 °C prior to assembly with the non-adhesive layer.

### Preparation of the bioadhesive microparticles:

For fabrication of the bioadhesive microparticles, a bioadhesive film was first prepared by casting, curing, and drying the precursor solution described above. The fully dried bioadhesive material was then cryogenically grinded at 30 Hz frequency for 2 min. The resulting bioadhesive microparticles were sealed in plastic bags with desiccant and stored at −20 °C until use.

### Preparation of the zwitterionic-interpenetrated elastomer:

10 w/w % hydrophilic PU (HydroMed™ D3, Advansource Biomaterials) and 0.1 w/w % benzophenone dissolved in ethanol/water mixture (95:5 v/v) was spin-coated at 200 rpm. The spin-coated film was dried under airflow overnight, then submerged into an aqueous solution containing 35 w/w % [2-(Methacryloyloxy)ethyl]dimethyl-(3-sulfopropyl)ammonium hydroxide (DMAPS) and 5 w/w % α-ketoglutaric acid for 10 min, followed by curing in a UV chamber (284 nm, 10 W power) for 1 h. The resultant film was thoroughly washed in a large volume of deionized water for 3 days to remove unreacted reagents, then thoroughly dried under airflow.

**Assembly of the multilayer patch:**

To combine the zwitterionic layer with the bioadhesive layer, a thin layer of 5 w/w % hydrophilic PU solution in ethanol/water mixture (95:5 v/v) was spin-coated at 400 rpm over the flat surface of the bioadhesive layer. The zwitterionic layer was then pressed on top and the entire assembly was thoroughly dried. The hydrophilic PU solution served as an adhesive between the zwitterionic layer and the bioadhesive layer by interpenetrating and drying between the two layers. To introduce the hydrophobic fluid layer, silicone oil (100 cSt viscosity) was first sterilized by filtration through a sterile membrane with 0.2 μm pore size to remove bacteria and other microorganisms. The sterilized silicone oil was then impinged on the micro-textured surface of the bioadhesive layer.

**Statistical analysis:**

MATLAB software was used to assess the statistical significance of all comparison studies in this work. Data distribution was assumed to be normal for all parametric tests, but not formally tested. In the statistical analysis for comparison between multiple samples, one-way ANOVA followed by Tukey's multiple comparison test were conducted with the threshold of $*p$  0.05, $**p$  0.01, and $***p$  0.001. In the statistical analysis between two data groups, a two-sample Student's $t$-test was used, and the significance threshold was placed at $*p$  0.05, $**p$  0.01, and $***p$  0.001.

Other experimental details are included in Supporting Information.

## Supplementary Material

Refer to Web version on PubMed Central for supplementary material.

## Acknowledgements

## References

[1]. U.S. Food and Drug Administration, Meeting of the General and Plastic Surgery Devices Panel. 2019, https://www.fda.gov/media/126211/download.

[2]. Annabi N, Yue K, Tamayol A, Khademhosseini A, Eur. J. Pharm. Biopharm 2015, 95, 27–39. [PubMed: 26079524]

[3]. Taboada GM, Yang K, Pereira M, Liu SS, Hu Y, Karp JM, Artzi N, Lee Y, Nat. Rev. Mater 2020, 5, 1–20.

[4]. Murrell ZA, Stamos MJ, Clinics in Colon and Rectal Surgery 2006, 19, 213–216. [PubMed: 20011323]

[5]. Papachristou DN, Fortner JG, The American Journal of Surgery 1979, 138, 399–402. [PubMed: 474876]

[6]. Mack MJ, JAMA 2001, 285, 568–572. [PubMed: 11176860]

[7]. Avery RK, Albadawi H, Akbari M, Zhang YS, Duggan MJ, Sahani DV, Olsen BD, Khademhosseini A, Oklu R, Sci. Transl. Med 2016, 8, 365.

[8]. Hu J, Altun I, Zhang Z, Albadawi H, Salomao MA, Mayer JL, Madhubhani LP, Hemachandra P, Rehman S, Oklu R, Adv. Mater 2020, 32, 2002611.

[9]. Reece TB, Maxey TS, Kron IL, The American Journal of Surgery 2001, 182, S40–S44.

[10]. Ryou M, Thompson CC, Techniques in Gastrointestinal Endoscopy 2006, 8, 33–37.

[11]. Spotnitz WD, Burks S, Transfusion 2008, 48, 1502–1516. [PubMed: 18422855]

[12]. Cui C, Wu T, Chen X, Liu Y, Li Y, Xu Z, Fan C, Liu W, Adv. Funct. Mater 2020, 2005689.

[13]. Yuk H, Varela CE, Nabzdyk CS, Mao X, Padera RF, Roche ET, Zhao X, Nature 2019, 575, 169–174. [PubMed: 31666696]

[14]. Wang Y, Shang L, Chen G, Sun L, Zhang X, Zhao Y, Sci. Adv 2020, 6, eaax8258. [PubMed: 32042897]

[15]. Duarte A, Coelho J, Bordado J, Cidade M, Gil M, Prog. Polym. Sci 2012, 37, 1031–1050.

[16]. O'Rorke RD, Pokholenko O, Gao F, Cheng T, Shah A, Mogal V, Steele TWJ, Biomacromolecules 2017, 18, 674–682. [PubMed: 28124557]

[17]. Lang N, Pereira MJ, Lee Y, Friehs I, Vasilyev NV, Feins EN, Ablasser K, O'Cearbhaill ED, Xu C, Fabozzo A, Padera R, Wasserman S, Freudenthal F, Ferreira LS, Langer R, Karp JM, del Nido PJ, Sci. Transl. Med 2014, 6, 218ra6.

[18]. Bhagat V, Becker ML, Biomacromolecules 2017, 18, 3009–3039. [PubMed: 28862846]

[19]. Chen X, Yuk H, Wu J, Nabzdyk CS, Zhao X, Proc. Natl. Acad. Sci. U. S. A 2020.

[20]. Epstein AK, Wong T-S, Belisle RA, Boggs EM, Aizenberg J, Proc. Natl. Acad. Sci. U. S. A 2012, 109, 13182–13187. [PubMed: 22847405]

[21]. Smith JD, Dhiman R, Anand S, Reza-Garduno E, Cohen RE, McKinley GH, Varanasi KK, Soft Matter 2013, 9, 1772–1780.

[22]. Sunny S, Cheng G, Daniel D, Lo P, Ochoa S, Howell C, Vogel N, Majid A, Aizenberg J, Proc. Natl. Acad. Sci. U. S. A 2016, 113, 11676–11681. [PubMed: 27688761]

[23]. Mao X, Yuk H, Zhao X, J. Mech. Phys. Solids 2020, 137, 103863.

[24]. Yuk H, Zhang T, Lin S, Parada GA, Zhao X, Nat. Mater 2016, 15, 190–196. [PubMed: 26552058]

[25]. Jiang S, Cao Z, Adv. Mater 2010, 22, 920–932. [PubMed: 20217815]

[26]. Smith RS, Zhang Z, Bouchard M, Li J, Lapp HS, Brotske GR, Lucchino DL, Weaver D, Roth LA, Coury A, Biggerstaff J, Sukavaneshvar S, Langer R, Loose C, Sci. Transl. Med 2012, 4, 153ra132.

[27]. Zhang L, Cao Z, Bai T, Carr L, Ella-Menye J, Irvin C, Ratner BD, Jiang S, Nat. Biotechnol 2013, 31, 553–556. [PubMed: 23666011]

[28]. Yue W-W, Li H-J, Xiang T, Qin H, Sun S-D, Zhao C-S, J. Membr. Sci 2013, 446, 79–91.

[29]. He H, Xiao Z, Zhou Y, Chen A, Xuan X, Li Y, Guo X, Zheng J, Xiao J, Wu J, J. Mater. Chem 2019, 7, 1697–1707.

[30]. Wu J, Lin W, Wang Z, Chen S, Chang Y, Langmuir 2012, 28, 7436–7441. [PubMed: 22512533]

[31]. Yu Y, Yuk H, Parada GA, Wu Y, Liu X, Nabzdyk CS, Youcef-Toumi K, Zang J, Zhao X, Adv. Mater 2019, 31, 1807101.

[32]. Carr L, Cheng G, Xue H, Jiang S, Langmuir 2010, 26, 14793–14798. [PubMed: 20731337]

[33]. Myers SR, Rothermel WS, Shaffer L, Surgical Endoscopy 2011, 25, 3043–3049. [PubMed: 21487874]

[34]. Baker RS, Foote J, Kemmeter P, Brady R, Vroegop T, Serveld M, Obesity Surgery 2004, 14, 1290–1298. [PubMed: 15603641]

[35]. Asada Y, Kisanuki A, Tsuneyoshi A, Marutsuka K, Hatakeyama K, Sumiyoshi A, Atherosclerosis 1996, 121, 45–53. [PubMed: 8678923]

[36]. Leslie DC, Waterhouse A, Berthet JB, Valentin TM, Watters AL, Jain A, Kim P, Hatton BD, Nedder A, Donovan K, Super EH, Howell C, Johnson CP, Vu TL, Bolgen DE, Rifai S, Hansen AR, Aizenberg M, Super M, Aizenberg J, Ingber DE, Nat. Biotechnol 2014, 32, 1134–1140. [PubMed: 25306244]

[37]. Hellebrekers B, Kooistra T, Br. J. Surg 2011, 98, 1503–1516. [PubMed: 21877324]

[38]. Stapleton LM, Steele AN, Wang H, Hernandez HL, Yu AC, Paulsen MJ, Smith AAA, Roth GA, Thakore AD, Lucian HJ, Totherow KP, Baker SW, Tada Y, Farry JM, Eskandari A, Hironaka CE, Jaatinen KJ, Williams KM, Bergamasco H, Marschel C, Chadwick B, Grady F, Ma M, Appel EA, Woo YJ, Nat. Biomed. Eng 2019, 3, 611–620. [PubMed: 31391596]

[39]. Miyashita S, Guitron S, Li S, Rus D, Science Robotics 2017, 2, eaao4369. [PubMed: 33157890]

[40]. Rus D, Tolley MT, Nat. Rev. Mater 2018, 3, 101–112.

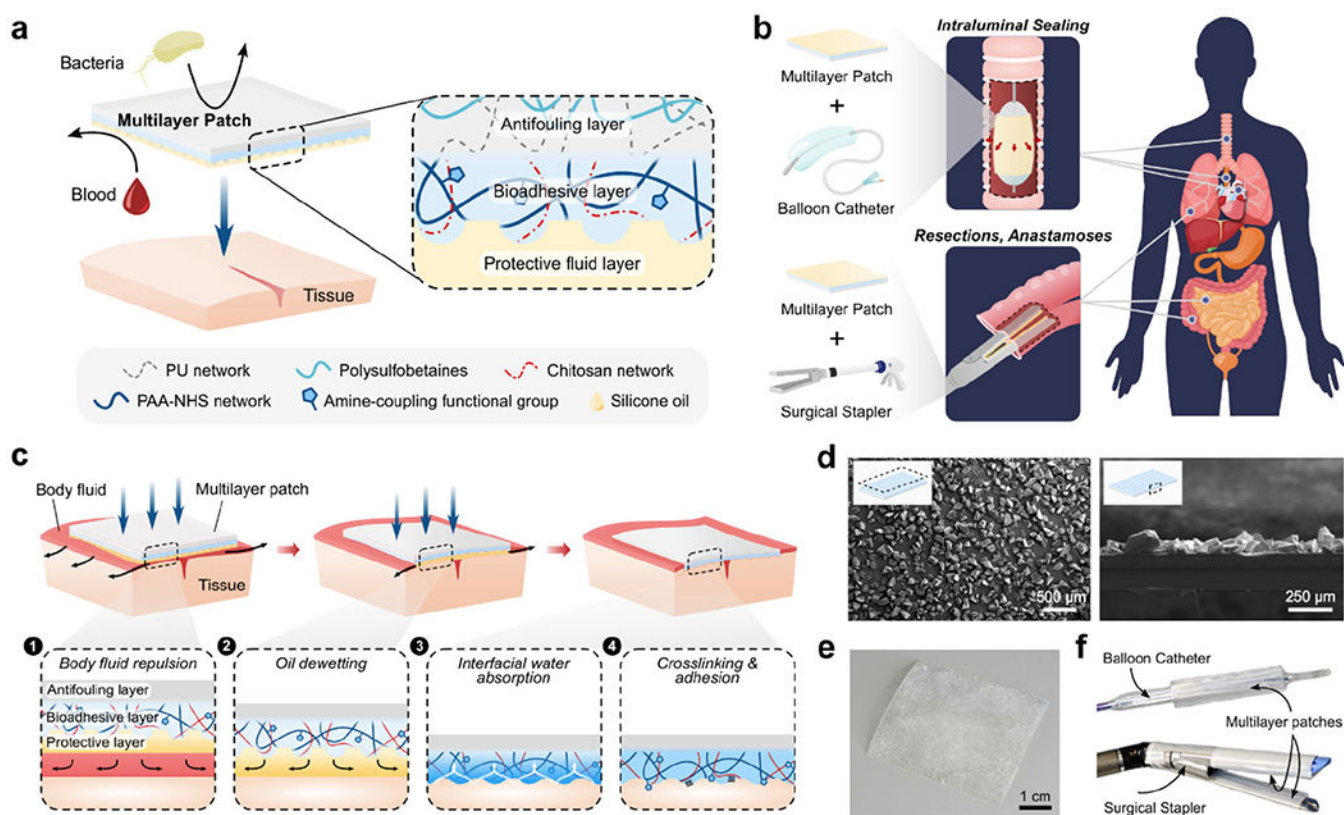[41]. Rafsanjani A, Zhang Y, Liu B, Rubinstein SM, Bertoldi K, Science Robotics 2018, 3, eaar7555. [PubMed: 33141681]

**Figure 1.**
a) Illustrated schematic of the multilayer composition of the bioadhesive patch. The patch comprises a textured bioadhesive fused with an antifouling polymer layer on the non-adherent side, and is wetted with a hydrophobic fluid layer on the adherent side to repel body fluids. b) Illustrated exemplary minimally invasive surgical applications of the multilayer patch via balloon catheters for intraluminal sealing of tube-shaped organs and structures, and surgical staplers for linear seals in resections and anastomoses. c) Schematic of the adhesion mechanism of the multilayer patch. (1) As the patch is maneuvered toward the tissue, the hydrophobic protective layer repels blood and prevents contamination of the bioadhesive layer. (2) Application of pressure exceeding 77.5 kPa drives dewetting of the oil from the bioadhesive layer. (3) The bioadhesive layer makes contact with the tissue surface and absorbs interfacial water immediately, forming temporary crosslinks. (4) Covalent bonds form between NHS ester functional groups in the bioadhesive layer for stable, long term adhesion. d) Scanning electron micrographs of a top-view (left) and a side-view (right) of the micro-textured surface of the bioadhesive layer. e) Photograph of the assembled multilayer patch. f) Multilayer patches loaded on a balloon catheter and surgical stapler.
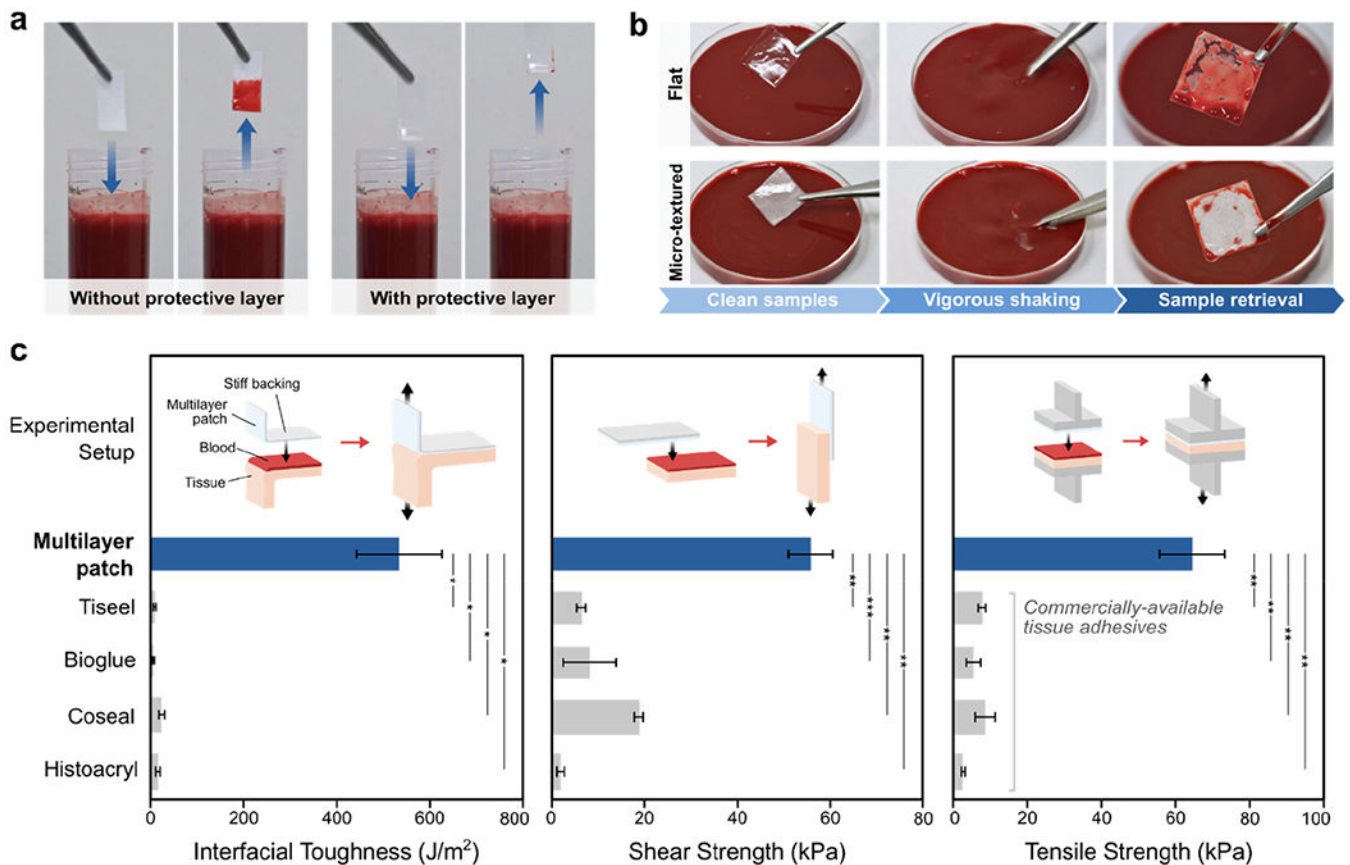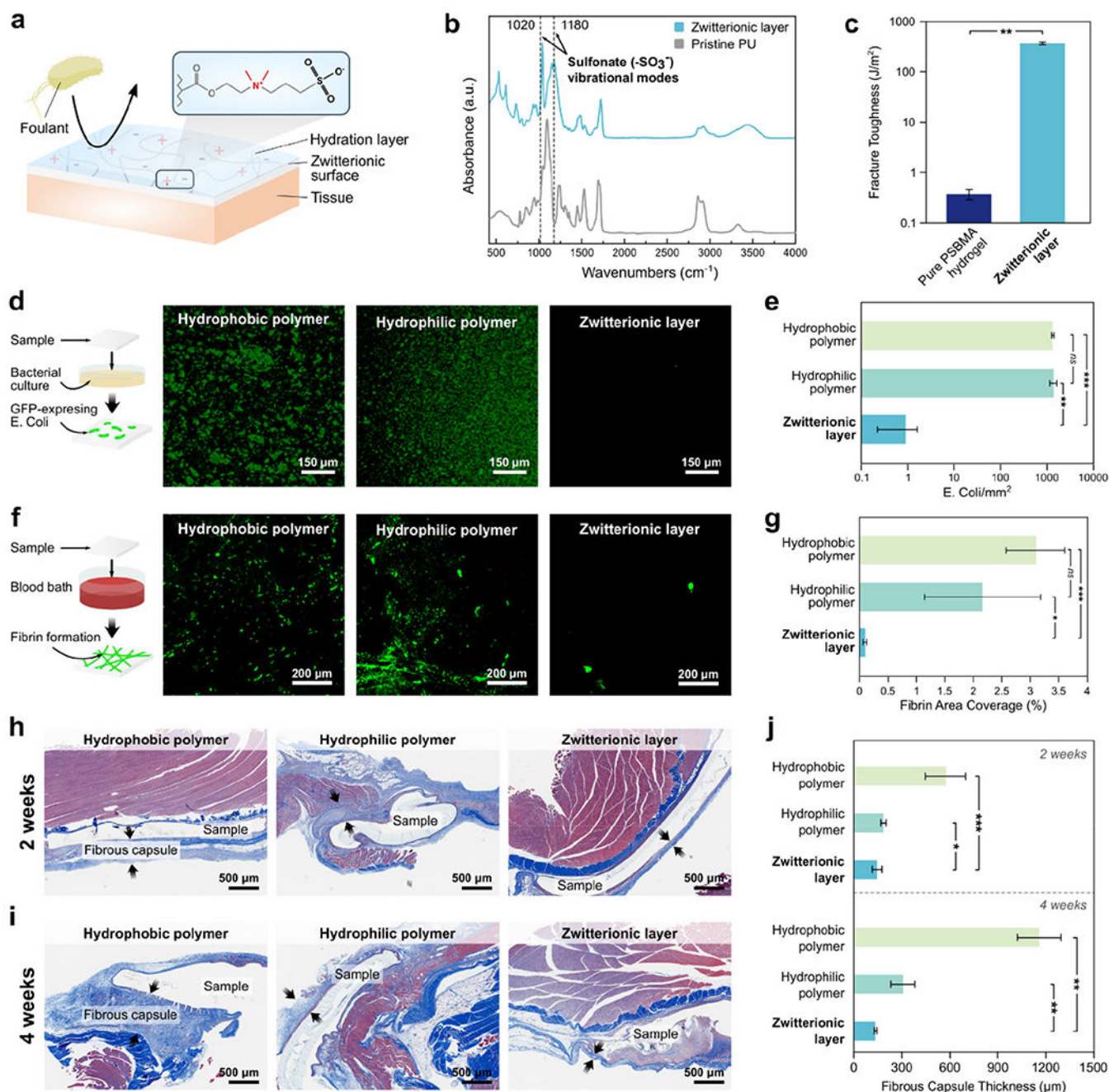
**Figure 2.**
a) Photographs of multilayer patches with and without the hydrophobic fluid layer before and after submerging in a porcine blood. b) Photographs of the multilayer patches with flat and micro-textured bioadhesive layers before and after vigorously shaking in a porcine blood bath. The multilayer patch containing a micro-textured bioadhesive layer exhibits greater stability and blood-repellent capacity of the hydrophobic fluid layer. c) Comparison of adhesion performances of the multilayer patch and various commercially-available tissue adhesives, adhered to porcine skin coated with porcine blood. Values represent the mean and the standard deviation ($n = 3$). $P$ values are determined by a Student's $t$-test; ns, not significant ($p > 0.05$); * $p$ 0.05; **$p$ 0.01; *** $p$ 0.001.

**Figure 3.**

*In vitro* and *in vivo* antifouling performance of the multilayer patch. a) Illustrated depiction of the antifouling mechanism of the zwitterionic-interpenetrated elastomer. Foulant adsorption is prevented due to the formation of a tightly bound hydration layer caused by electrostatic interactions between water molecules and the charged zwitterionic polymers. b) FTIR spectra of the zwitterionic layer and unmodified pristine hydrophilic PU; peaks at $1020 \text{ cm}^{-1}$ and $1180 \text{ cm}^{-1}$ correspond to vibrational modes of the sulfonate group ($-SO_3^-$). c) Fracture toughness of a pure zwitterionic hydrogel ($0.35 \text{ J m}^{-2}$) and the zwitterionic-interpenetrated elastomer layer ($420 \text{ J m}^{-2}$). d) Representative fluorescent micrographs of

GFP-expressing *E. Coli* adhered to a hydrophobic polymer (PDMS), a hydrophilic polymer (PU), and the zwitterionic layer following 24 h incubation. e) The number of adhered *E. Coli* per $mm^2$ for each substrate. f) Representative fluorescent micrographs of fibrin network formation on a hydrophobic polymer (PDMS), a hydrophilic polymer (PU), and the zwitterionic layer after 60 min of exposure to porcine whole blood spiked with fluorescently-tagged fibrinogen. h) Fibrin area coverage (%) for each substrate. h,i) Representative histological images stained with Masson's trichrome for *in vivo* rat dorsal subcutaneous implantation of patches with non-adhesive faces comprised of a hydrophobic polymer (PDMS, left), a hydrophilic polymer (PU, middle), and the zwitterionic layer (right) after 2 weeks (h) and 4 weeks (i). j) Fibrous capsule thickness formed around the implanted samples after *in vivo* the implantation. Values in (c,e,g,j) represent the mean and the standard deviation ($n = 4$). *P* values are determined by a Student's *t*-test; * $p$ 0.05; ** $p$ 0.01; *** $p$ 0.001.
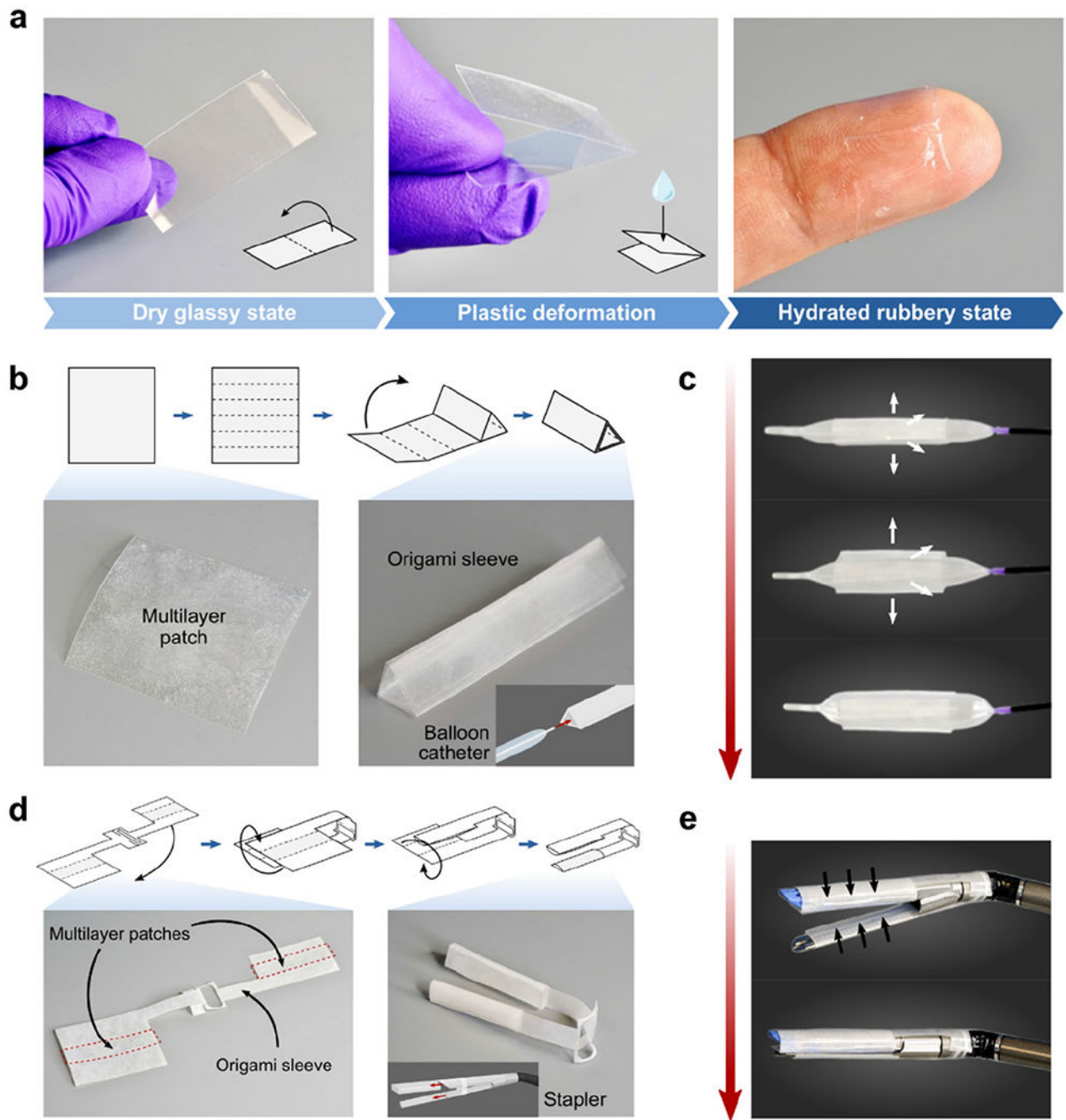
**Figure 4.**
Design and assembly of the multilayer patch for various surgical end effectors. a) Photographs showing the multilayer patch in the plastically-deformable dry glassy state. Upon hydration, the folded patch transitions to the rubbery state and becomes a soft conformable hydrogel. b) Origami-based design and fabrication of a triangular sleeve for integration of the multilayer patch with a balloon catheter. c) Photographs showing the deployment mechanism using an esophageal balloon catheter. Increasing inflation pressure in the balloon induces radial expansion and unfurling of the multilayer patch. d) Origami-

based design and fabrication of a dualsleeve adaptor for integration of the multilayer patch with an articulating linear stapler. The multilayer patches are denoted by the red dashed lines. e) Photographs showing the deployment mechanism using an articulating linear stapler. Actuation of the stapler compresses the anvil and cartridge units together, triggering adhesion.
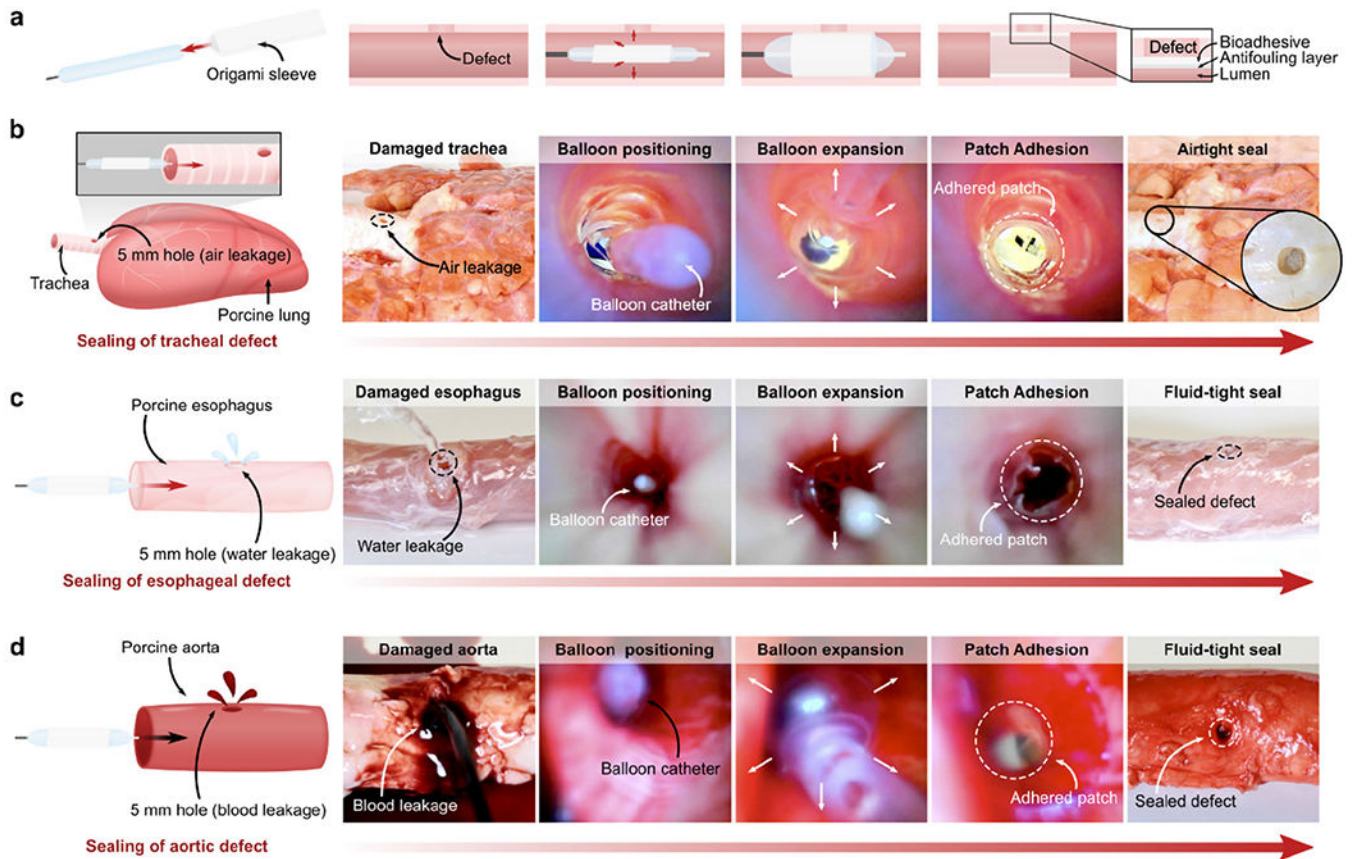
**Figure 5.**
*Ex vivo* demonstrations of minimally invasive delivery and application of the multilayer bioadhesive patch by balloon catheters. a) Schematic illustrations of the origami patch integration and endoluminal delivery process using a balloon catheter. b) Macroscopic and endoscopic photographs of the airtight sealing of a porcine tracheal defect (5-mm hole) by the multilayer patch delivered and applied via a Foley catheter. c) Macroscopic and endoscopic photographs of the fluid-tight sealing of a porcine esophageal defect (5-mm hole) by the patch delivered and applied via an esophageal catheter. d) Macroscopic and endoscopic photographs of the fluid-tight sealing of a porcine aortic defect (5-mm hole) by the patch delivered and applied via a Foley catheter.
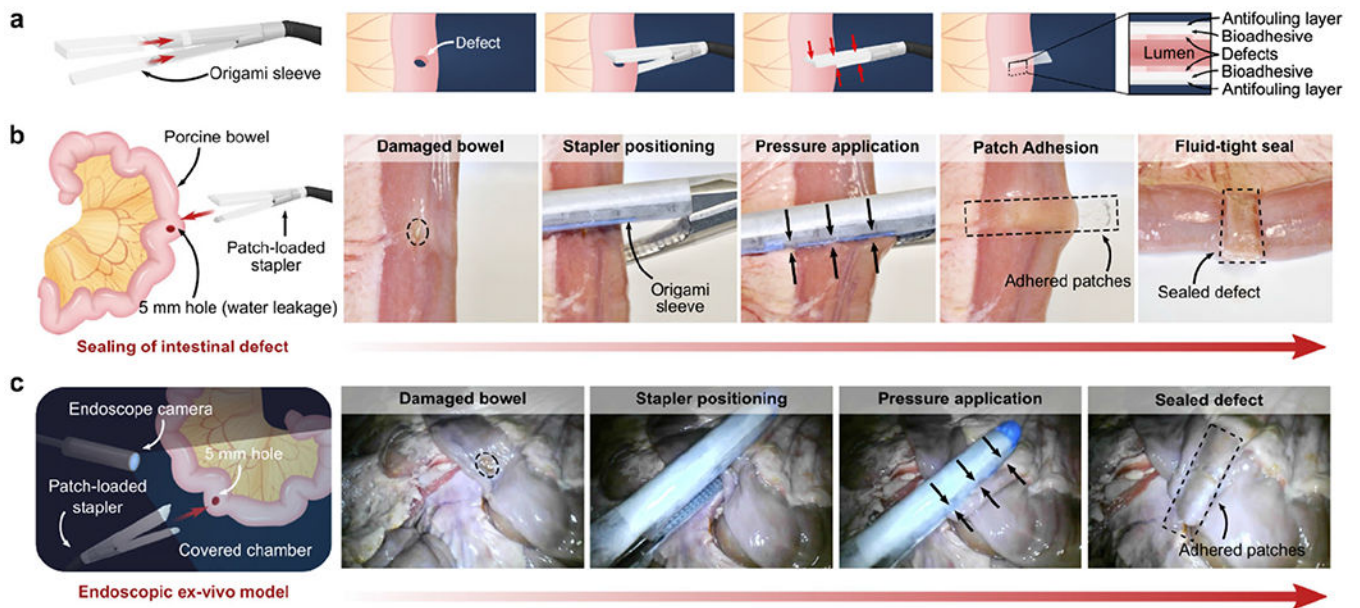
**Figure 6.**
*Ex vivo* demonstrations of minimally invasive delivery and application of the multilayer bioadhesive patch to create using a surgical stapler. a) Schematic illustrations of the patch integration and delivery process using an articulating linear stapler. b) Macroscopic photographs of the fluid-tight linear sealing of a porcine intestinal defect (5-mm hole) by patches delivered and applied via an articulating linear stapler. c) Endoscopic footage of the sealing of a porcine intestinal defect (5-mm hole) performed in a dark, covered chamber to mimic a minimally invasive surgical procedure.